

# Tunable plasmonic thin magneto-optical wave plate

A. V. BARYSHEV<sup>1,3,\*</sup> AND A. M. MERZLIKIN<sup>1,2,4</sup>

<sup>1</sup>All-Russia Research Institute of Automatics, 127055 Moscow, Russia

<sup>2</sup>Institute for Theoretical and Applied Electromagnetics, Moscow 125412, Russia

<sup>3</sup>Ioffe Physical-Technical Institute, St. Petersburg 194021, Russia

<sup>4</sup>Moscow Institute of Physics and Technology, Moscow 141700, Russia

\*Corresponding author: baryshev@vniia.ru

Received 22 January 2016; revised 15 March 2016; accepted 13 April 2016; posted 11 May 2016 (Doc. ID 258081); published 7 June 2016

**Planar periodic plasmonic structures encased in a magnetic host revealed an unexpected polarization transformation. In the proposed thin periodic gold–garnet layer, the near fields strongly modify (enhance) the magneto-optical response of garnet. We show that the configuration of near fields in the magnetized layer can be engineered so that the layer converts the linear polarization to elliptical (or circular) or rotates the plane of polarization over a large angle in the transmission (or Faraday) geometry. Since the helicity of elliptically (circularly) polarized light (or the polarization rotation angle) is altered by reversing the magnetization of garnet, the considered plasmonic structure acts as a tunable wave plate.** © 2016 Optical Society of America

**OCIS codes:** (160.3820) Magneto-optical materials; (230.2240) Faraday effect; (250.5403) Plasmonics; (310.6628) Subwavelength structures, nanostructures.

<http://dx.doi.org/10.1364/JOSAB.33.001399>

## 1. INTRODUCTION

Achievements in nanophotonics demonstrated artificial materials supporting optical resonances of different natures. Among the representatives are metallic structures supporting surface plasmon polaritons (SPPs)—the collective excitations of the charge density of free carriers in metals due to light waves. The foremost features of SPPs are the surface and localized surface plasmon resonances (SPRs and LSPRs, respectively) [1,2]. Owing to these resonances, plasmonic structures introduce the strong evanescent near fields into modern research directions [3] such as miniature circuitry [4,5], high-accuracy biosensing [6,7], and SPP lasers [8].

Amplification of the near field through SPR and LSPR is also shown to be useful for tailoring properties of magneto-optical (MO) materials comprising plasmonic subsystems [9]. Fundamental and practical interest in artificial MO structures is to enhance magneto-optical (MO) responses of existing bulk MO materials [9–15] and to control the flow of light by external magnetic fields [9,16,17–20]. Needless to say, the application of plasmonic MO structures is a challenging task due to intriguing possibilities of (i) miniaturization through near-field light confinement and (ii) nanosecond timescale modulation by the magnetic field.

Interest in plasmonic MO structures is reflected in works demonstrating modified spectra of conventional MO films [11–24], composites [25,26], and periodic structures [27–35].

In these works, the SPR- or LSPR-related increase of the MO response is observed in the Faraday (or Kerr) rotation spectra. It is worth mentioning that the reported phenomenon of enhanced polarization rotation cannot be called the enhanced Faraday (or nonreciprocal magneto-optical) effect because the observed LSPR-enhanced angle of polarization rotation is a reciprocal phenomenon by its nature [30]. A complete theory describing mechanisms behind the enhancement of polarization rotation is disputable thus far.

Our previous studies on plasmonic noble metal–garnet composite films allowed us to conceive how their material and structural parameters influence spectral positions and intensities of the LSPR bands and the related enhancement of the MO response and to interpret its peculiarities [26,30]. Anticipating giant MO responses, in the present work, we start from a discussion of experimental 100 nm thick plasmonic MO samples and then theoretically study analogous gold–garnet structures with planar square lattices of 100 nm Au spheres and engineer their LSPR. Finally, we find a specific interference regime for two spectrally neighboring LSPR. For a calculated optimized structure, we show that the fields of scattered waves configure so that they interfere destructively, thus strongly regulating the amplitude and phase of the transmitted wave. The near-field interference in the magnetized structure leads to transformation of the linearly polarized wave to the circularly polarized one upon light propagation. The proposed tunable

plasmonic thin wave plate can modulate the helicity of the circularly polarized light when reversing the magnetization of garnet.

## 2. SAMPLES, EXPERIMENT, AND SIMULATION

Experimental gold–bismuth-substituted garnet (Au–Bi:YIG) thin layers were fabricated by electron lithography and ion beam sputtering. First, a two-dimensional square array of Au disks was fabricated from a 30 nm thick Au film on top of a quartz substrate. Then, the Au array was subjected to a treatment at a temperature of 750°C required for crystallization of Bi:YIG. At this step, the initial Au disks are most likely melted and converted to spheroids. This preliminary step was necessary for diminishing distortions at the Au/Bi:YIG interfaces at the next step: sputtering Bi:YIG on top of Au/quartz and annealing as-sputtered film for Bi:YIG crystallization. Fabricated polycrystalline garnet had a composition of  $\text{Bi}_1\text{Y}_2\text{Fe}_5\text{O}_{12}$ .

The final samples comprised a two-dimensional (2D) square lattice of Au particles fabricated on a 1 mm thick quartz substrate [Fig. 1(a)], which were encased in a Bi:YIG film fabricated on top of quartz/2D lattice [Fig. 1(b)]. The 2D lattice had periods of  $D = 200, 300$ , and  $400$  nm, and the Bi:YIG film had a thickness of  $d \approx 100$  nm. As we discuss below, the Au–Bi:YIG samples in our study were made to satisfy LSPR in the visible range.

Structural properties of the samples were evaluated using a Jeol JSM-6700 scanning electron microscope. It is most likely that, after temperature treatment, the Au particles were close to spheroids with a height of 30 nm and diameters of 109 nm (for the sample with  $D = 200$  nm), 103 nm ( $D = 300$  nm), and 89 nm ( $D = 400$  nm) estimated from images like that shown in Fig. 1(a). According to our analysis, the above-mentioned parameters had fluctuations in their magnitudes of about  $\pm 5$  nm. The height of 30 nm corresponded to the thickness of sputtered Au. This may explain certain deviations in spectral

positions and intensities of the experimental and calculated LSRR peaks.

Optical responses were measured using a Shimadzu UV-3100PC spectrophotometer and an apparatus for magneto-optical studies (Neo Ark BH-M600VIR-FKR-TU). Experimental transmission and polarization rotation spectra were obtained with 5 nm spectral resolution; the angular divergence of the incident light beam was less than  $1^\circ$ , and the light spot diameter was less than 2 mm. The experiments were done for collimated polarized light beams at normal incidence, where a ray of light traveled through a sample only once (with an account of reflections from the slab's interfaces). The magnitude of  $\mathbf{H} = \pm 2$  kOe was chosen to saturate the magnetization of Bi:YIG. For more details on the peculiarities of the responses of the plasmonic MO structures, see Ref. [30].

Rigorous numerical analysis was done by using Comsol Multiphysics 4.3a. Dispersion of dielectric parameters for Au were taken from Ref. [36] and that of the dielectric tensor of Bi:YIG both for the diagonal and non-diagonal elements was reconstructed from fabricated Bi:YIG [37].

Numerical analysis was done for analogous structures comprising 2D lattices of spherical 100 nm Au particles embedded into the center of a 150 nm thick Bi:YIG film ( $d = 150$  nm) in air [Fig. 1(c)]. The periods of the Au lattices  $D$  were the same as that of the experimental samples. Such a model was chosen for the sake of simplicity, where the near fields around Au spheres penetrated into the symmetrical dielectric background. This model reflected the main optical properties of the experimental samples. To reach regimes of different wave plates in the performed calculations, the only varied parameter was the lattice constant  $D$ . Note that, for the considered geometry of normal incidence, the light from the measured and analyzed range did not diffract from the studied samples into the air and the substrate, except for the cases of  $D = 350$  nm for  $\lambda < 600$  nm and  $D = 400$  nm for  $\lambda < 650$  nm that correspond to emergence of diffraction orders.

To analyze field configurations, the magnitudes of the  $E_x$  and  $E_y$  components of the electric field were traced along section lines  $\mathbf{S1}$ – $\mathbf{S3}$  through the depth of the calculation model,  $\mathbf{S1}$  and  $\mathbf{S2}$  were the lines tangent to the Au sphere, and  $\mathbf{S3}$  was the line crossing the model in between two neighboring Au spheres at  $D/2$ . The incident wave had  $E_y$  polarization and a magnitude of  $E_y = 1$ , the angle of polarization rotation of the emerging wave was evaluated in the definitions of Comsol as  $\theta(\mathbf{H}) = \text{atan}(\text{emw.E}_x/\text{emw.E}_y)$ , and the phase shift between  $E_x$ - and  $E_y$ -components was  $\varphi(\mathbf{H}) = \arg(\text{emw.E}_y) - \arg(\text{emw.E}_x)$ .

## 3. RESULTS AND DISCUSSION

### A. Transmission Spectra and Faraday Rotation

In Fig. 2, transmission and MO spectra of the Au–Bi:YIG samples exhibited the well-known features of the LSPR-related absorption bands and the corresponding peaks in the spectra of polarization rotation. Curves 1–3 correspond respectively to the samples with  $D = 200, 300$ , and  $400$  nm, and curves 4 stand for properties of the single Bi:YIG film for comparison. Measured [Fig. 2(a)] and calculated [Fig. 3(a)] transmission spectra for a range of  $D$  illustrate the following optical features

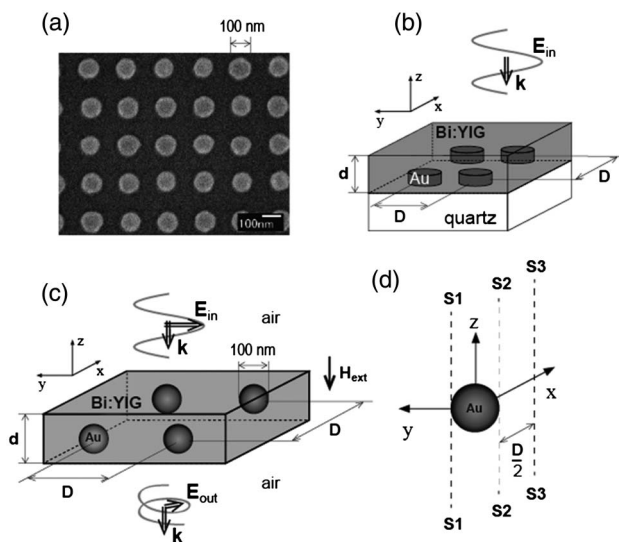


**Fig. 1.** Experimental samples and calculation model: (a) a scanning electron microscope image of a square Au lattice, (b) a sketch of the experimental Au–Bi:YIG sample, (c) a calculation model, and (d) an Au sphere and section lines through the calculation model.

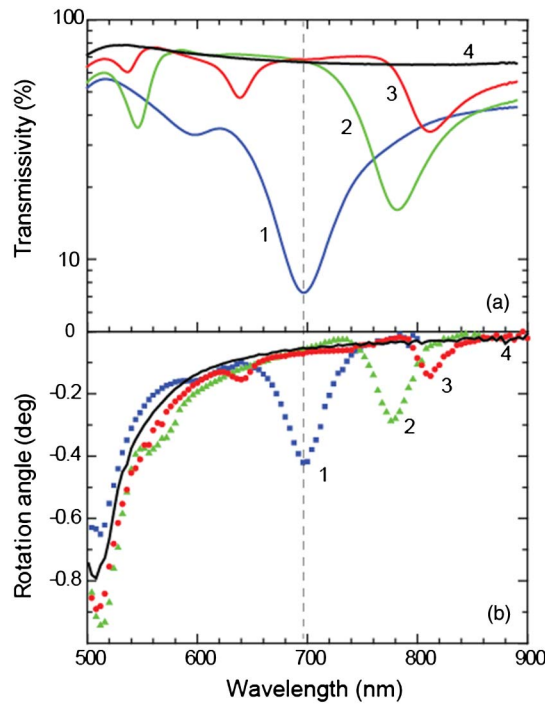


**Fig. 2.** (a) Experimental transmittance and (b) polarization rotation spectra of Au-Bi:YIG samples: curves 1 for  $D = 200$  nm, curves 2 for  $D = 300$  nm, and curves 3 for  $D = 400$  nm. Curves 4 show spectra of a reference 100 nm thick Bi:YIG film with no inclusions of Au.

of Au – Bi:YIG layers: (i) there are two main LSPR peaks in the spectral range of interest, (ii) the spectral position of the short-wavelength (SW) peak exhibits a minor shift as  $D$  decreases, and (iii) the long-wavelength (LW) peak experiences a large shift and begins to overlap with the SW peak for  $D < 200$  nm. The LW peak is defined by the lattice period  $D$  and, in our case, Au scatterers interact via their dipolar fields in the regime of the evanescent diffraction order as studied by Meier *et al.* [38]. This phenomenon is experimentally studied by Lamprecht *et al.* [39], showing that the  $D$ -dependent peak of absorption by Au particles experienced a redshift as  $D$  reached a critical grating constant.

As for the spectral position of the SW peak ( $\lambda_{SW}$ ), it is defined by the parameters of the single scatterer and is attributed to the resonance of the scatterer polarizability at  $\text{Real}\{\epsilon_{Au}(\omega)\} + 2 \cdot \epsilon_{Bi:YIG}(\omega) = 0$ . For example,  $\text{Real}(\epsilon_{Au}(\text{at } \lambda = 610 \text{ nm})) \approx -9.4$  [36] and  $2 \cdot \epsilon_{Bi:YIG}(\text{at } \lambda_{SW} = 610 \text{ nm}) \approx 10.4$  [37]; see the SW peak in the calculated spectrum with  $D = 300$  nm. This deviation can be explained by the limited thickness of the Bi:YIG film, where Au scatterers sense not only the garnet background but also the garnet/air interface. It should be mentioned that, for an Au-Bi:YIG sample with nonperiodic distribution of Au nanoparticles having different sizes (20–80 nm), the only LSPR absorption band associated with the scatterer polarizability takes a spectral position of  $\approx 640$  nm [40].

Spectral positions of the experimental LW peaks ( $\lambda_{LW}$ ) are short- or long-wavelength shifted as compared with the calculated  $\lambda_{LW}$  (see Figs. 2 and 3). Misfits between spectral positions of the LW peaks in the experimental and calculated spectra are most likely due to the existence of an air shell or oxides of the

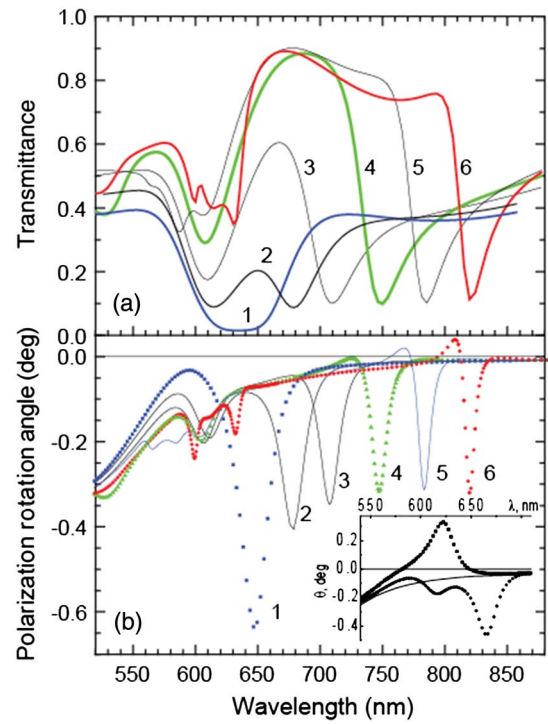


**Fig. 3.** (a) Calculated transmittance and (b) polarization rotation spectra of 2D Au-Bi:YIG layers: curves 1 to 6 correspond to  $D = 200, 220, 250, 300, 350,$  and  $400$  nm, respectively. The inset illustrates the sign reversal of polarization rotation: a peak of positive rotation corresponds to  $D = 180$  nm, peaks of negative rotation  $-D = 210$  nm, and the solid curve presents the Faraday rotation angle of a reference 100 nm thick Bi:YIG film with no inclusions of Au.

atoms composing garnet, providing a difference in the dielectric background at the interface between Au and Bi:YIG. Also, the shape of Au nanoparticles and the spacing between them and the thickness of the Bi:YIG coat around each Au particle were ideally kept in the calculation that was not the case of the experiment.

It is instructive to analyze the relation between  $\lambda_{LW}$  and  $D$ . For this we utilize consideration of the grating effects on plasmon excitation given in Refs. [38,39]. Provided that the  $E_y$  wave excites dipoles radiating mainly along the  $x$ -axis (into the lateral plane of the Au-Bi:YIG samples) [see Fig. 1(c)], let us assume the following diffraction relation  $n_{eff} = \lambda_{LW}/D$ , where  $n_{eff}$  is an effective refractive index of an Au-Bi:YIG layer. Circles in Fig. 4 illustrate the quantity of  $n_{eff}$  calculated in the framework of the Maxwell-Garnett theory (MGT):

$$n_{eff}^2 = n_{Bi:YIG}^2 \left[ 1 - \frac{3V(n_{Bi:YIG}^2 - \text{Real}(\epsilon_{Au}))}{2n_{Bi:YIG}^2 + \text{Real}(\epsilon_{Au}) + V(n_{Bi:YIG}^2 - \text{Real}(\epsilon_{Au}))} \right],$$

where  $n_{Bi:YIG}^2$  and  $\text{Real}(\epsilon_{Au})$  are the permittivities of corresponding materials for the wavelengths of  $\lambda_{LW}$  taken from Fig. 3(a), and  $V$  is the volume fraction of Au. Other curves demonstrate the quantities of  $n_{eff}$  extracted from the experimental (triangles) and calculated (squares) spectra. In Fig. 4, one can see a good agreement between the experimental and



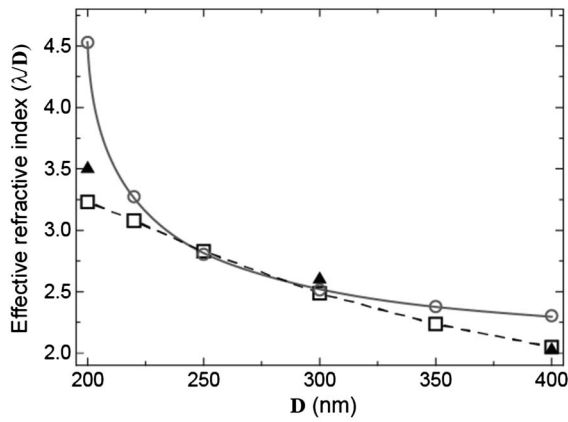


**Fig. 4.** Effective refractive index of Au-Bi:YIG layers versus the lattice constant: MGT (circles), quantities obtained in experiment (triangles) and in calculation (squares).

calculated  $n_{\text{eff}}$  with their deviation from MGT. This together with a consideration illustrated in Fig. 6 supports that LW peaks originated from an increase in plasmon damping due to the grating effect (or surface lattice resonance).

The features corresponding to SW and LW peaks were also observed in spectra of polarization rotation  $\theta(\mathbf{H})$ , see Fig. 3(b). The experimental and calculated spectra were in a good agreement. First, the number of peaks and their spectral shifts were the same; see, for example, curves 2 and 4 in Figs. 2 and 3, respectively. Second, the gain in the magnitude of the rotation angle was larger for the smaller  $D$ . Third,  $\theta(\mathbf{H})$  was not only enhanced for the LSPR wavelengths but also decreased and tended to reverse its sign; see Fig. 2(b) and curves 4–6 in Fig. 3(b). Indeed, the sign reversal of  $\theta(\mathbf{H})$  was obtained for  $D = 180$  nm; see the inset to Fig. 3(b). It is evident that this resulted from simultaneous light coupling to the SW and LW resonances. Further simulation in a range of  $D$  providing the opposite signs for  $\theta(\mathbf{H})$  showed that there existed a critical period in the vicinity of  $D = 193$  nm. For such structure, transmittance was strongly suppressed due to cumulative damping of the incident wave by SW and LW LSPR. In this regime, the magnitude and sign of  $\theta(\mathbf{H})$  changed abruptly from  $90^\circ$  to  $-90^\circ$  (Fig. 5) in the vicinity of  $\lambda = 634$  nm.

### B. Mechanism of Enhanced Polarization Rotation

Let us examine the correspondence between the  $\mathbf{E}_y$  field distribution through the calculated model, the magnitude of transmittance, and the enhancement of  $\theta(\mathbf{H})$ . For a model with  $D = 300$  nm, Figs. 6(a)–6(c) illustrate these  $\mathbf{E}_y$  field distributions along section lines constructed as shown in Fig. 1(d). Figures 6(a) and 6(b) show the LW- and SW-LSPR-modified  $\mathbf{E}_y$  field distributions, respectively, together with the dielectric profile of the Au-Bi:YIG layers along section lines  $\mathbf{S1}$  and  $\mathbf{S2}$ . To illustrate plasmon excitation, a phase corresponding to the maximum of the  $\mathbf{E}_y$  field for section line  $\mathbf{S1}$  is selected (for  $\mathbf{S2}$  and  $\mathbf{S3}$ , the same phase).

Along section lines  $\mathbf{S1}$  and  $\mathbf{S2}$ , the LW excitation ( $\lambda_{\text{LW}} = 750$  nm) was characterized by the stronger near field on the surface of the Au sphere ( $\mathbf{E}_y = 11$  V/m for  $\mathbf{S1}$ ) than

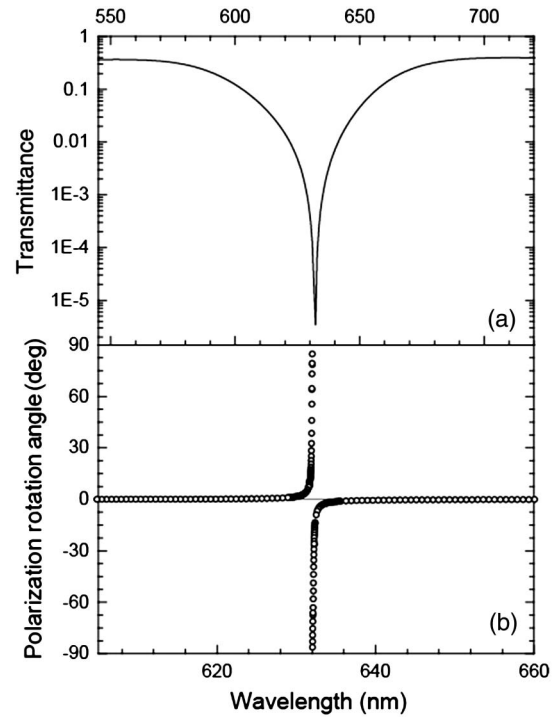


**Fig. 5.** (a) Calculated transmittance and (b) polarization rotation spectra of an Au-Bi:YIG layer with a critical lattice constant  $D = 193$  nm.

that for the SW excitation ( $\lambda_{\text{SW}} = 607$  nm,  $\mathbf{E}_y = 4.5$  V/m for  $\mathbf{S1}$ ). This was associated with the stronger decrease of transmittance of the propagating  $\mathbf{E}_y$  wave at the LW excitation and resulted in the larger polarization rotation. Figure 6(c) presents the  $\mathbf{E}_y$  field distribution for  $\lambda = 685$  nm (between LW and SW), where  $\mathbf{E}_y$  was 3.2 V/m for  $\mathbf{S1}$ , and transmittance was as high as  $T = 0.9$  [see Fig. 3(a), curve 4]. One may conclude that the rise of  $\mathbf{E}_y$  for  $\lambda = 685$  nm was due to plasmon excitation, but with this the  $\mathbf{E}_y$  wave was scattered forward in phase (see the  $\mathbf{E}_y$  field distribution along section lines  $\mathbf{S1}$ – $\mathbf{S3}$ ).

Figure 6 shows that the observed enhancement of  $\theta(\mathbf{H})$  was not only due to the excitation of plasmons, but it was also due to the transmission attenuation via absorption due to the SW resonance and via diffraction-amplified absorption due to the LW resonance. Clear manifestation of this conclusion was the  $\mathbf{E}_y$  field distribution for  $D = 193$  nm at  $\lambda = 632$  nm where the propagating  $\mathbf{E}_y$  modes were extremely attenuated [Fig. 6(d)] upon propagation inside the Au-Bi:YIG layer. Scattering of the incident  $\mathbf{E}_y$  wave into the transmitted  $\mathbf{E}_y$  wave was strongly suppressed; however, the  $\mathbf{E}_x$  component born inside the Au-Bi:YIG layer (namely, on the Au/Bi:YIG interface) due to MO activity augmented over the  $\mathbf{E}_y$  component. With accounts of the phase shift between the  $\mathbf{E}_x$  and  $\mathbf{E}_y$  components, all this resulted in the rise of  $\theta(\mathbf{H})$  up to  $\pm 90^\circ$ .

Thus, the LSPR-affected gain in  $\theta(\mathbf{H})$  is connected with the suppression of the  $\mathbf{E}_y$  component and the phase shift between the tunneling  $\mathbf{E}_y$  component and the born via magneto-optical activity  $\mathbf{E}_x$  component of the emerging wave. This mechanism confirms conclusions of Ref. [30] discussing the reciprocal

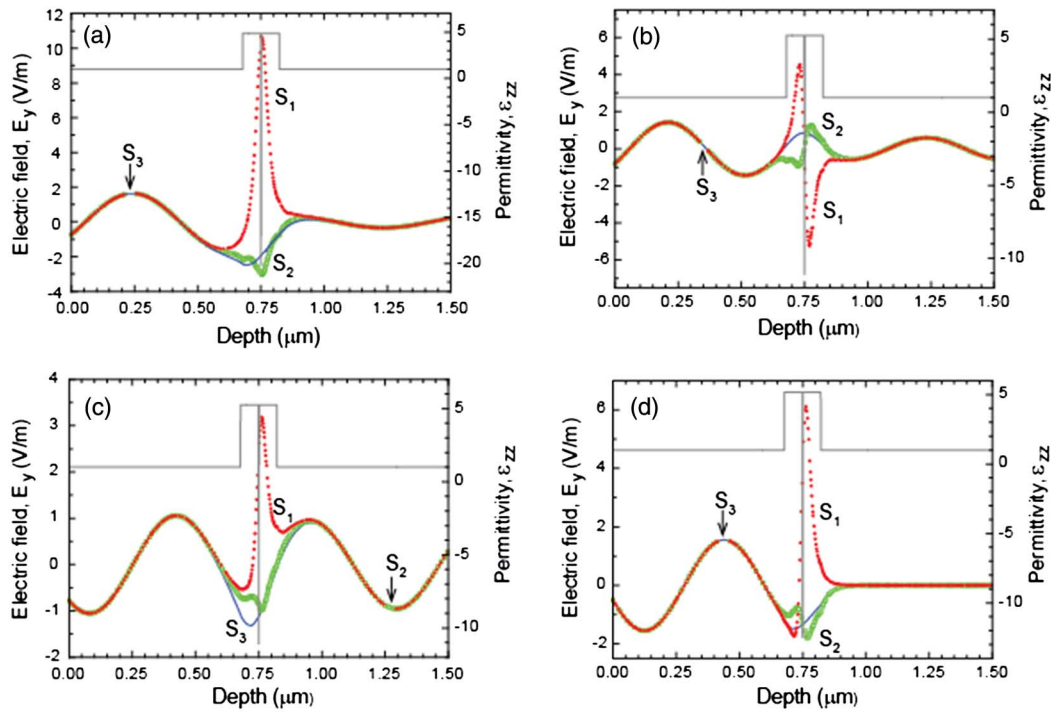


**Fig. 6.** Calculated  $E_y$  field profiles along section lines shown in Fig. 1(d). For  $D = 300$  nm, the distributions are at (a)  $\lambda = 750$  nm, (b) 607 nm, and (c) 685 nm. For  $D = 193$  nm, plot (d) illustrates transmission suppression due to destructive interference of the  $E_y$  mode with  $\lambda = 633$  nm.

nature of the LSPR-enhanced polarization rotation of plasmonic MO.

### C. Tunable Near-Field Wave Plate

To illustrate possible actions of the Au-Bi:YIG structure in our study, we calculated spectra presenting the polarization state of transmitted light  $\theta(H_+)$ ,  $\theta(H_-)$ ,  $\phi(H_+)$ , and  $\phi(H_-)$ , when magnetizing the structure in the opposite directions. For magnetization  $H_+$  as shown in Fig. 1(c), Fig. 7 shows spectra of the 150 nm thick Au-Bi:YIG layer with the 2D lattice made of 100 nm Au spheres arranged with  $D = 193$  nm in the vicinity of  $\lambda = 634$  nm. Calculations revealed that the incident linearly polarized light with frequencies from the LSPR range was rotated over a large angle up to  $45^\circ$  (arrows 1) or converted to elliptically polarized light (arrows 2) and circularly polarized light (arrows 3).

Importantly, the angle of polarization rotation (the angle between the main axis of the polarization ellipse and the direction of the incident  $E$ -field) was rotated clockwise [positive magnitude of  $\theta(H_+)$ ], the opposite sign as compared to that of Bi:YIG and counterclockwise [negative magnitude of  $\theta(H_+)$ ], the same sign as for Bi:YIG for  $\lambda < 634$  nm and  $\lambda > 634$  nm, respectively. A sharp flip-over of  $\theta(H_+)$  associated with strong damping of the incident  $E_y$  component and with prevailing the emerging  $E_x$  component was observed [see a curve of  $\theta_2(H_+)$ ]. Obviously, the direction of the main axis of the polarization ellipse can be modified by the lattice constants, and the helicity of the  $E$ -field circulation can be controlled by the direction of magnetization of Bi:YIG. Note that, for the nonmagnetized structure, light propagated with no change in its polarization state.

Provided that a fabricated sample will have a deviation of  $D$ , which will possibly diverge within a particular sample from a designed value, it is important to understand quantitatively tendencies in the spectra of polarization rotation and phase shift for slightly different values of  $D$ . Arrows 2 in Fig. 7 indicate a wavelength of 634 nm, where phase shifts are equal

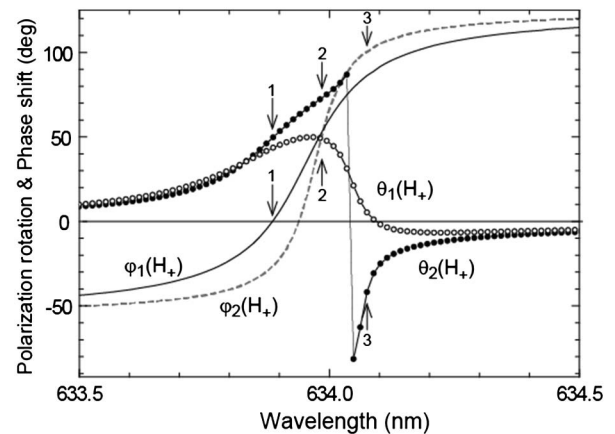


**Fig. 7.** Characteristics of a tunable near-field wave plate. Curves  $\theta_1(+H)$  and  $\theta_2(+H)$  correspond to different values of  $D$  in the vicinity of  $D = 193$  nm ( $D_1 = 193.1$  and  $D_2 = 193.2$ ); curves  $\phi_1(+H)$  and  $\phi_2(+H)$  stand for phase shifts between  $E_x$  and  $E_y$  components. Arrows 1 indicate the regime where the linear polarization rotated over an angle of  $\theta_1(+H) \approx 45^\circ$ , arrows 2 show the regime of elliptical polarization where phase shifts for different values of  $D$  are equal, and arrows 3 stand for circularly polarized light. The direction of the magnetic field ( $+H$ ) is as shown in Fig. 1(c).

$\varphi_1(\mathbf{H}_+) = \varphi_2(\mathbf{H}_+) \approx 55^\circ$  for two realizations of the 2D lattice of Au–Bi:YIG with  $\mathbf{D}_1 = 193.1$  nm and  $\mathbf{D}_2 = 193.2$  nm, and the rotation angles were  $\theta_1(\mathbf{H}_+) \approx 50^\circ$  and  $\theta_2(\mathbf{H}_+) \approx 80^\circ$ . This result illustrates that light emerging from the Au–BiYIG layer can have the main axis of polarization ellipse rotated over a large angle, and the primary angle of polarization rotation and the helicity of polarization rotation can be modulated by the external magnetic field.

#### 4. CONCLUSION

The measured and calculated spectra presented peculiarities of the plasmonic magneto-optical system modifying the polarization state of incident radiation. Utilizing two-dimensional gold–bismuth-substituted garnet thin layers with the square symmetry, we (i) interpreted the plasmon-modified enhancement of polarization rotation and (ii) found the critical lattice constant providing different wave-plate regimes.

These regimes were a consequence of simultaneous light coupling to two localized plasmon resonances for the 2D plasmonic lattice embedded in the magnetized garnet. It is the condition of crossing two LSPRs that attenuates propagation of the incident wave, when strongly localizing light at the Au–Bi:YIG interface, and modifies the initial polarization state. We believe that the current study provides a way for tailoring plasmonic magneto-optical structures for optical applications with requirements for modulating the polarization state on the nanosecond timescale. Also, a further search for systems based on other metals or alloys and demonstrating active (electro-, thermo-optical, photorefractive, etc.) plasmonics can substantially increase the applicability range of our results.

**Funding.** Foundation of Perspective Investigations, Russia (7/004/2013–2018); Ministry of Education, Culture, Sports, Science and Technology (MEXT, Japan); Program to Foster Young Researchers in Cutting-Edge Interdisciplinary Research; Grants-in-Aid for Scientific Research (24510178).

**Acknowledgment.** The authors are grateful to H. Uchida, T. V. Murzina, V. Zayets, and M. Inoue for helpful discussions.

#### REFERENCES AND NOTES

- H. Raether, *Surface Plasmons on Smooth and Rough Surfaces and on Grating* (Springer, 1988).
- Y. Teng and E. A. Stern, "Plasma radiation from metal grating surfaces," *Phys. Rev. Lett.* **19**, 511–514 (1967).
- S. A. Maier, *Plasmonics: Fundamentals and Applications* (Springer, 2007).
- S. I. Bozhevolnyi, V. S. Volkov, E. Devaux, J.-Y. Laluet, and T. Ebbesen, "Channel plasmon subwavelength waveguide components including interferometers and ring resonators," *Nature* **440**, 508–511 (2006).
- T. W. Ebbesen, C. Genet, and S. I. Bozhevolnyi, "Surface-plasmon circuitry," *Phys. Today* **61**(5), 44–50 (2008).
- R. Slavik, J. Homola, and H. Vaisocherova, "Advanced biosensing using simultaneous excitation of short and long range surface plasmons," *Meas. Sci. Technol.* **17**, 932–938 (2006).
- A. V. Baryshev, A. M. Merzlikin, and M. Inoue, "Efficiency of optical sensing by a plasmonic photonic-crystal slab," *J. Phys. D* **46**, 125107 (2013).
- P. Berini and I. De Leon, "Surface plasmon–polariton amplifiers and lasers," *Nat. Photonics* **6**, 16–24 (2011).
- M. Inoue, M. Levy, and A. Baryshev, eds., *Magnetophotonics: From Theory to Applications* (Springer, 2013).
- M. Inoue, R. Fujikawa, A. Baryshev, A. Khanikaev, P. B. Lim, H. Uchida, O. Aktsipetrov, A. Fedyanin, T. Murzina, and A. Granovsky, "Magnetophotonic crystals," *J. Phys. D* **39**, R151 (2006).
- Z. Wu, M. Levy, V. J. Fratello, and A. M. Merzlikin, "Gyrotropic photonic crystal waveguide switches," *Appl. Phys. Lett.* **96**, 051125 (2010).
- S. I. Khartsev and A. M. Grishin, "High performance latching-type luminescent magneto-optical photonic crystals," *Opt. Lett.* **36**, 2806–2808 (2011).
- S. M. Baek, A. V. Baryshev, and M. Inoue, "Multiple Bragg diffraction in magnetophotonic crystals," *Appl. Phys. Lett.* **98**, 101111 (2011).
- H. Marinchio, R. Carminati, A. García-Martín, and J. J. Sáenz, "Magneto-optical Kerr effect in resonant subwavelength nanowire gratings," *New J. Phys.* **16**, 015007 (2014).
- A. Christofi, N. Stefanou, and N. Papanikolaou, "Periodic structures of magnetic garnet particles for strong Faraday rotation enhancement," *Phys. Rev. B* **89**, 214410 (2014).
- A. Khanikaev, A. Baryshev, M. Inoue, A. Granovsky, and A. Vinogradov, "Two-dimensional magnetophotonic crystal: exactly solvable model," *Phys. Rev. B* **72**, 035123 (2005).
- A. M. Merzlikin, A. P. Vinogradov, M. Inoue, and A. B. Granovsky, "Giant photonic Hall effect in magnetophotonic crystals," *Phys. Rev. E* **72**, 046603 (2005).
- K. Fang, Z. Yu, V. Liu, and S. Fan, "Ultracompact nonreciprocal optical isolator based on guided resonance in a magneto-optical photonic crystal slab," *Opt. Lett.* **36**, 4254–4256 (2011).
- V. V. Temnov, G. Armelles, U. Woggon, D. Guzatov, A. Cebollada, A. García-Martín, J. M. García-Martín, T. Thomay, A. Leitenstorfer, and R. Bratschkitsch, "Active magneto-plasmonics in hybrid metal–ferromagnet structures," *Nat. Photonics* **4**, 107–111 (2010).
- V. I. Belotelov, L. E. Kreilkamp, I. A. Akimov, A. N. Kalish, D. A. Bykov, S. Kature, V. J. Yallapragada, A. Venu Gopal, A. M. Grishin, S. I. Khartsev, M. Nur-E-Alam, M. Vasiliev, L. L. Doskolovich, D. R. Yakovlev, K. Alameh, A. K. Zvezdin, and M. Bayer, "Plasmon-mediated magneto-optical transparency," *Nat. Commun.* **4**, 2128 (2013).
- G. S. Krinchik, E. E. Chepurova, and T. E. Kraeva, "Magneto-optical effects in nickel and permalloy associated with frustrated total internal reflection," *J. Exp. Theor. Phys.* **62**, 156–160 (1985).
- V. E. Kochergin, A. Y. Toporov, and M. Valeiko, "Polariton enhancement of the Faraday magneto-optic effect," *J. Exp. Theor. Phys. Lett.* **68**, 400–403 (1998).
- C. Hermann, V. A. Kosobukin, G. Lampel, J. Peretti, V. I. Safarov, and P. Bertrand, "Surface-enhanced magneto-optics in metallic multilayer films," *Phys. Rev. B* **64**, 235422 (2001).
- G. Shemer and G. Markovich, "Enhancement of magneto-optical effects in magnetite near gold surfaces," *J. Phys. Chem. B* **106**, 9195–9197 (2002).
- S. Tomita, T. Kato, S. Tsunashima, S. Iwata, M. Fujii, and S. Hayashi, "Magneto-optical Kerr effects of yttrium–iron garnet thin films incorporating gold nanoparticles," *Phys. Rev. Lett.* **96**, 167402 (2006).
- Y. Mizutani, H. Uchida, Y. Masuda, A. V. Baryshev, and M. Inoue, "Magneto-optical plasmonic Bi:YIG composite films with Ag and Au–Ag alloy particles," *J. Magn. Soc. Jpn.* **33**, 481–484 (2009).
- J. B. González-Díaz, A. García-Martín, G. Armelles, D. Navas, M. Vázquez, K. Nielsch, R. B. Wehrspohn, and U. Gösele, "Enhanced magneto-optics and size effects in ferromagnetic nanowire arrays," *Adv. Mater.* **19**, 2643–2647 (2007).
- A. B. Khanikaev, A. V. Baryshev, A. A. Fedyanin, A. B. Granovsky, and M. Inoue, "Anomalous Faraday effect of a system with extraordinary optical transmittance," *Opt. Express* **15**, 6612–6622 (2007).
- B. Sepúlveda, J. B. González-Díaz, A. García-Martín, L. M. Lechuga, and G. Armelles, "Plasmon-induced magneto-optical activity in nano-sized gold disks," *Phys. Rev. Lett.* **104**, 147401 (2010).
- A. V. Baryshev, H. Uchida, and M. Inoue, "Peculiarities of plasmon-modified magneto-optical response of gold–garnet structures," *J. Opt. Soc. Am. B* **30**, 2371–2376 (2013).

31. J. Y. Chin, T. Steinle, T. Wehls, D. Dregely, T. Weiss, V. I. Belotelov, B. Stritzker, and H. Giessen, "Nonreciprocal plasmonics enables giant enhancement of thin-film Faraday rotation," *Nat. Commun.* **4**, 1599 (2013).
32. N. Maccaferri, A. Berger, S. Bonetti, V. Bonanni, M. Kataja, Q. H. Qin, S. van Dijken, Z. Pirzadeh, A. Dmitriev, J. Nogués, J. Akerman, and P. Vavassori, "Tuning the magneto-optical response of nanosize ferromagnetic Ni disks using the phase of localized plasmons," *Phys. Rev. Lett.* **111**, 167401 (2013).
33. K. Lodewijks, N. Maccaferri, T. Pakizeh, R. K. Dumas, I. Zubritskaya, J. Akerman, P. Vavassori, and A. Dmitriev, "Magnetoplasmonic design rules for active magneto-optics," *Nano Lett.* **14**, 7207–7214 (2014).
34. N. Maccaferri, X. Inchausti, A. García-Martín, J. Carlos Cuevas, D. Tripathy, A. O. Adeyeye, and P. Vavassori, "Resonant enhancement of magneto-optical activity induced by surface plasmon polariton modes coupling in 2D magnetoplasmonic crystals," *ACS Photon.* **2**, 1769–1779 (2015).
35. D. Floess, J. Y. Chin, A. Kawatani, D. Dregely, H. U. Habermeier, T. Weiss, and H. Giessen, "Tunable and switchable polarization rotation with non-reciprocal plasmonic thin films at designated wavelengths," *Light* **4**, e284 (2015).
36. E. D. Palik, *Handbook of Optical Constants of Solids* (Academic, 1985).
37. Optical constants for the fabricated thin Bi:YIG films were evaluated by a J. A. Woollam Co. ellipsometer.
38. M. Meier, A. Wokaun, and P. F. Liao, "Enhanced fields on rough surfaces: dipolar interactions among particles of sizes exceeding the Rayleigh limit," *J. Opt. Soc. Am. B* **2**, 931–949 (1985).
39. B. Lamprecht, G. Schider, R. T. Lechner, H. Ditlbacher, J. R. Krenn, A. Leitner, and F. R. Aussenegg, "Metal nanoparticle gratings: influence of dipolar particle interaction on the plasmon resonance," *Phys. Rev. Lett.* **84**, 4721–4724 (2000).
40. R. Fujikawa, A. V. Baryshev, J. Kim, H. Uchida, and M. Inoue, "Contribution of the surface plasmon resonance to optical and magneto-optical properties of a Bi:YIG–Au nanostructure," *J. Appl. Phys.* **103**, 07D301 (2008).